

Nuclear pasta in hot neutron-star matter and proto-neutron stars

Jian Zhou¹, Junbo Pang¹, Hong Shen^{1,*}, and Jinniu Hu^{1,†}
¹ School of Physics, Nankai University, Tianjin 300071, China

We investigate nuclear pasta phases appearing in hot neutron-star matter based on the compressible liquid-drop model, where the matter consists of a dense liquid phase and a dilute gas phase separated by a sharp interface. The surface tension is calculated self-consistently from the Thomas-Fermi approximation, and it depends on temperature and isospin asymmetry. We employ relativistic mean-field models with different symmetry energy slopes to describe nuclear interactions. It is found that the TM1e model with a small symmetry energy slope of $L = 40$ MeV predicts various pasta shapes at low temperatures, while the TM1 model with $L = 110.8$ MeV yields only the droplet configuration up to the crust-core transition density. We examine the occurrence and influence of pasta phases in proto-neutron stars with a constant entropy per baryon. These pasta phases may occur in the inner crust with a thickness of about 1.2 km, playing an important role in the thermal evolution of the star.

I. INTRODUCTION

A proto-neutron star (PNS) is the compact object formed after the gravitational collapse of a massive stellar core [1–3]. It represents a fascinating transitional phase in stellar evolution, preceding the formation of cold neutron stars. After its formation in a core-collapse supernova, the PNS cools through deleptonization and neutrino emission. Within tens of seconds, neutrinos can escape freely from the PNS as the entropy steadily decreases [4, 5]. During the cooling process, the PNS contracts rapidly and heavy nuclei may appear in the surface region [6, 7]. The formation of heavy nuclei indicates a transition from uniform matter to a nonuniform crust. This stage is characterized by extreme physical conditions that challenge our understanding of nuclear physics and the thermal evolution of compact stars.

The structure and composition of the PNS are studied using the equation of state (EOS) of hot nuclear matter in β -equilibrium, referred to as hot neutron-star matter. The EOS plays a decisive role in understanding astrophysical phenomena, such as core-collapse supernova explosions, PNS cooling, and various properties of neutron stars [8–10]. Over the past decades, astronomical observational technologies have achieved significant advances, which have greatly improved our understanding of neutron-star properties [11–13]. These observations provide a wealth of information for constraining physics of matter under extreme conditions. The first direct detection of gravitational waves from a binary black hole merger, known as GW150914 [14], launched a new era of gravitational-wave astronomy. The observations of compact binary mergers by the LIGO and Virgo detectors have provided valuable constraints on the EOS and its underlying theoretical framework. It is well known that the tidal deformability of neutron stars can be inferred from gravitational-wave observations, although a large uncertainty remains from both the measurements and theoretical analyses. The milestone gravitational wave event GW170817 [15, 16] from a

binary neutron-star merger provided an estimate of the tidal deformability and constrained the radius for canonical neutron stars with masses around $1.4 M_{\odot}$ [17–20]. Furthermore, several precise measurements of massive pulsars [21–24], require the maximum neutron-star mass to be larger than $2 M_{\odot}$, which provides a stringent constraint on the EOS of neutron stars. The recent observations by NICER (Neutron Star Interior Composition Explorer) for PSR J0030+0451 [25, 26] and PSR J0740+6620 [27, 28] have provided simultaneous measurements of the mass and radius of neutron stars, which offer further constraints on the EOS of dense matter. The nuclear many-body approach employed in studies of the EOS should be compatible with current constraints from astrophysical observations and with various properties of finite nuclei.

In this work, we employ the relativistic mean-field (RMF) approach to describe nuclear interactions. Currently, the RMF approach is recognized as a specific realization of covariant density functional theory, providing a consistent relativistic framework applicable to nuclear physics and astrophysics [10, 29, 30]. To explore the influence of nuclear symmetry energy on neutron-star matter, we adopt the RMF models with the TM1 parametrization [31] and its extended version TM1e [32–34]. It is noteworthy that the TM1 and TM1e models have the same isoscalar properties but exhibit significantly different behaviors regarding nuclear symmetry energy. The slope parameters of symmetry energy are respectively $L = 40$ MeV (TM1e) and $L = 110.8$ MeV (TM1). It is well known that the slope parameter L plays a crucial role in determining the neutron-star radius and the crust structure [33, 35]. Furthermore, these two models have been applied to construct general EOSs for astrophysical simulations such as core-collapse supernovae and binary neutron-star mergers [34, 36].

At low temperatures and subsaturation densities, heavy nuclei are formed in nonuniform matter to reduce the free energy of the system [37–39]. As the density increases close to the crust-core transition, nonspherical pasta phases may appear, arising from the competition between surface and Coulomb energies [35]. As a result, the stable nuclear shape in nonuniform matter may change from spherical droplets to rods, slabs, tubes, and bubbles with increasing baryon density. Possibly, nuclear pasta phases exist both in core-collapse super-

* shennankai@gmail.com

† hujinniu@nankai.edu.cn

nova matter with fixed proton fraction and in the inner crust of neutron stars, where the matter is neutron-rich and in β -equilibrium. Over the past decades, nuclear pasta phases have been studied using various methods, such as the liquid-drop model [40, 41] and the Thomas-Fermi approximation [42–46]. It is noteworthy that nuclear symmetry energy and its density dependence significantly affect the pasta phase structure and determine its density region [35, 41, 42, 44]. In addition, the structure and properties of nuclear pasta can alter thermal conductivity and neutrino transport in a PNS, thereby influencing the PNS cooling process. It is of great interest and importance to investigate nuclear pasta phases in hot neutron-star matter.

We have two aims in this article. The first is to investigate the properties of pasta phases occurring in hot neutron-star matter. Specifically, we examine the effects of nuclear symmetry energy through a comparison of results from the TM1 and TM1e models. The second is to explore the impact of pasta phases on PNS properties, employing a constant entropy approach. To describe nuclear pasta phases at finite temperatures, we adopt the compressible liquid-drop (CLD) method with RMF models for nuclear interactions. Generally, the Wigner-Seitz approximation is employed to simplify the calculations, in which the whole space is divided into equivalent cells of specific geometric symmetry. Within each Wigner-Seitz cell, a dense liquid coexists with a dilute gas of free nucleons and α particles, with the two phases separated by a sharp interface. The equilibrium conditions for two coexisting phases are derived by minimizing the total free energy, which includes surface and Coulomb contributions. These conditions, which incorporate finite-size effects, differ from the Gibbs conditions for phase equilibrium. When finite-size effects are neglected, the CLD method reduces to a bulk matter calculation satisfying the Gibbs equilibrium conditions.

The surface tension τ plays a key role in determining the structure of pasta phases [41, 43]. Generally, τ depends on the temperature T and the proton fraction of the dense liquid phase Y_p^L [47, 48]. The surface tension can be derived by using the Thomas-Fermi approximation for a one-dimensional nuclear system consisting of protons and neutrons [43, 49]. In our previous works [41, 48], we calculated the surface tension τ at each given T and Y_p^L , a computationally expensive procedure. For simplicity, in the present calculation, we employ a parameterized surface tension τ , with parameters fitted to the results of the Thomas-Fermi approximation.

This article is organized as follows. In Sec. II, we briefly review the RMF approach and the CLD method used for describing nuclear pasta phases in hot neutron-star matter. In Sec. III, we present the results for nuclear pasta in hot neutron-star matter and discuss their occurrence and influence in a PNS. The conclusions are given in Sec. IV.

II. FORMALISM

We investigate nuclear pasta phases appearing in hot neutron-star matter based on the CLD method [41, 48], where the RMF model is adopted for the nuclear interaction [32].

For the self-containment of this paper, we provide a brief description of the RMF model and the CLD method.

A. RMF model

In the RMF approach, nucleons interact via the exchange of mesons, including the isoscalar-scalar meson σ , isoscalar-vector meson ω , and isovector-vector meson ρ . The Lagrangian density of neutron-star matter consisting of neutrons, protons, and electrons can be written as

$$\begin{aligned} \mathcal{L} = & \sum_{i=p,n} \bar{\psi}_i [i\gamma_\mu \partial^\mu - (M + g_\sigma \sigma) \\ & - \gamma_\mu \left(g_\omega \omega^\mu + \frac{g_\rho}{2} \tau_a \rho^{a\mu} \right)] \psi_i \\ & + \frac{1}{2} \partial_\mu \sigma \partial^\mu \sigma - \frac{1}{2} m_\sigma^2 \sigma^2 - \frac{1}{3} g_2 \sigma^3 - \frac{1}{4} g_3 \sigma^4 \\ & - \frac{1}{4} W_{\mu\nu} W^{\mu\nu} + \frac{1}{2} m_\omega^2 \omega_\mu \omega^\mu + \frac{1}{4} c_3 (\omega_\mu \omega^\mu)^2 \\ & - \frac{1}{4} R_{\mu\nu}^a R^{a\mu\nu} + \frac{1}{2} m_\rho^2 \rho_\mu^a \rho^{a\mu} + \Lambda_V (g_\omega^2 \omega_\mu \omega^\mu) (g_\rho^2 \rho_\mu^a \rho^{a\mu}) \\ & + \bar{\psi}_e (i\gamma_\mu \partial^\mu - m_e) \psi_e, \end{aligned} \quad (1)$$

where $W^{\mu\nu}$ and $R^{a\mu\nu}$ denote the antisymmetric field tensors for ω^μ and $\rho^{a\mu}$, respectively. The isospin Pauli matrices are denoted by τ_a , with the third component $\tau_3 = 1$ for protons and $\tau_3 = -1$ for neutrons. With the mean-field approximation, the meson fields are treated as classical fields, replacing the field operators with their expectation values. The nonvanishing expectation values of meson fields are denoted as $\sigma = \langle \sigma \rangle$, $\omega = \langle \omega^0 \rangle$, and $\rho = \langle \rho^{30} \rangle$. In homogeneous neutron-star matter at finite temperature, it is straightforward to derive the equations of motion for nucleons and mesons [48]. These coupled equations can be solved self-consistently. The thermodynamic quantities of interest include the energy density given by

$$\begin{aligned} \epsilon = & \sum_{i=p,n,e} \frac{1}{\pi^2} \int_0^\infty dk k^2 \sqrt{k^2 + m_i^{*2}} (f_{i+}^k + f_{i-}^k) \\ & + \frac{1}{2} m_\sigma^2 \sigma^2 + \frac{1}{3} g_2 \sigma^3 + \frac{1}{4} g_3 \sigma^4 + \frac{1}{2} m_\omega^2 \omega^2 \\ & + \frac{3}{4} c_3 \omega^4 + \frac{1}{2} m_\rho^2 \rho^2 + 3\Lambda_V (g_\omega^2 \omega^2) (g_\rho^2 \rho^2), \end{aligned} \quad (2)$$

the entropy density written as

$$\begin{aligned} s = & - \sum_{i=p,n,e} \frac{1}{\pi^2} \int_0^\infty dk k^2 [f_{i+}^k \ln f_{i+}^k \\ & + (1 - f_{i+}^k) \ln(1 - f_{i+}^k) + f_{i-}^k \ln f_{i-}^k \\ & + (1 - f_{i-}^k) \ln(1 - f_{i-}^k)], \end{aligned} \quad (3)$$

and the pressure given by

$$P = \sum_{i=p,n,e} \frac{1}{3\pi^2} \int_0^\infty dk \frac{k^4}{\sqrt{k^2 + m_i^{*2}}} (f_{i+}^k + f_{i-}^k) - \frac{1}{2} m_\sigma^2 \sigma^2 - \frac{1}{3} g_2 \sigma^3 - \frac{1}{4} g_3 \sigma^4 + \frac{1}{2} m_\omega^2 \omega^2 + \frac{1}{4} c_3 \omega^4 + \frac{1}{2} m_\rho^2 \rho^2 + \Lambda_V (g_\omega^2 \omega^2) (g_\rho^2 \rho^2). \quad (4)$$

The free energy density is calculated from

$$f = \epsilon - Ts. \quad (5)$$

Here, $m_p^* = m_n^* = M + g_\sigma \sigma$ is the effective nucleon mass, while $m_e^* = m_e$ denotes the electron mass. f_{i+}^k and f_{i-}^k represent the occupation probabilities of particle and antiparticle at momentum k , which are given by the Fermi–Dirac distribution,

$$f_{i\pm}^k = \left\{ 1 + \exp \left[\left(\sqrt{k^2 + m_i^{*2}} \mp \nu_i \right) / T \right] \right\}^{-1}. \quad (6)$$

where ν_i denotes the kinetic part of the chemical potential μ_i . For nucleons, $\nu_i = \mu_i - g_\omega \omega - \frac{g_\rho}{2} \tau_3 \rho$, whereas for electrons, $\nu_e = \mu_e$. The number density of species i is calculated from

$$n_i = \frac{1}{\pi^2} \int_0^\infty dk k^2 (f_{i+}^k - f_{i-}^k). \quad (7)$$

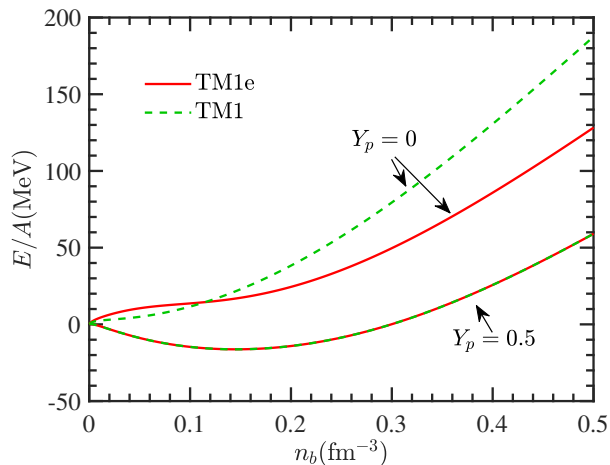


FIG. 1. Energy per baryon E/A of symmetric nuclear matter and pure neutron matter as a function of the baryon number density n_b in the TM1e and TM1 models.

The RMF models with various parameterizations have been widely and successfully used to describe infinite nuclear matter, finite nuclei, and stellar matter in extreme isospin conditions [29, 30]. In this study, we investigate the effects of the symmetry energy on nuclear pasta in hot neutron-star matter using two different RMF models: the TM1 and TM1e models [32, 34]. The original TM1 model, proposed by Sugahara

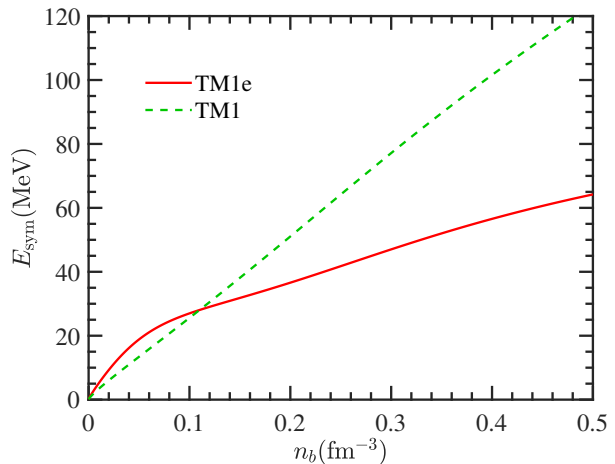


FIG. 2. Symmetry energy E_{sym} as a function of the baryon number density n_b in the TM1e and TM1 models.

and Toki [31], provides a satisfactory description of finite nuclei, including unstable nuclei, and has also been widely used to construct the EOS for supernova simulations [10, 39, 50]. An extended TM1 model, referred to as the TM1e model, was proposed by Bao *et al.* [32] and subsequently applied to construct the EOS table for astrophysical simulations [34]. For completeness, we present the coupling constants of the TM1e and original TM1 models in Table I. It is noteworthy that, while the TM1e and original TM1 models share the same isoscalar properties, they exhibit different behaviors in the symmetry energy. Compared to the original TM1 model, an additional ω – ρ coupling term characterized by the coupling Λ_V is introduced in the TM1e model, which plays a crucial role in determining the density dependence of the symmetry energy [32, 49]. In the TM1e model, at saturation density, the symmetry energy $E_{\text{sym}} = 31.38$ MeV and the slope parameter $L = 40$ MeV are obtained, which fall well within the constraints from various observations [10]. In contrast, the original TM1 model yields $E_{\text{sym}} = 36.89$ MeV and $L = 110.8$ MeV, which predict rather large neutron-star radii.

In Fig. 1, we plot the energy per baryon E/A for symmetric nuclear matter and pure neutron matter as a function of baryon density n_b . It is seen that the behaviors of symmetric nuclear matter are the same between the TM1e and TM1 models, while significant differences are evident in pure neutron matter. In Fig. 2, we plot the symmetry energy E_{sym} as a function of n_b . The TM1e model exhibits slightly larger E_{sym} at low densities but much smaller E_{sym} at high densities compared to the TM1 model. This discrepancy primarily arises from the different symmetry energy slopes L in these models. By making a detailed comparison between the TM1e and TM1 models, we can conveniently explore how the symmetry energy and its density dependence influence the properties of nuclear pasta in stellar matter.

TABLE I. Coupling constants of the TM1e and TM1 models.

Model	g_σ	g_ω	g_ρ	g_2 (fm $^{-1}$)	g_3	c_3	Λ_V
TM1e	10.0289	12.6139	13.9714	-7.2325	0.6183	71.3075	0.0429
TM1	10.0289	12.6139	9.2644	-7.2325	0.6183	71.3075	0.0000

B. CLD method at finite temperature

We employ the CLD model to describe the pasta phases in hot neutron-star matter. The Wigner-Seitz approximation is adopted for simplifying the calculations, in which the whole space is divided into charge-neutral cells with assumed geometric shapes. In the CLD model, the matter within the Wigner-Seitz cell is assumed to consist of a dense liquid (L) and a dilute gas (G) phase, separated by a sharp interface. Generally, the geometric shapes are likely to vary from droplet to rod, slab, tube, and bubble with increasing baryon density.

At a given temperature T and average baryon density n_b , the equilibrium state of neutron-star matter can be determined by minimizing the total free energy density of the system among all configurations considered [32, 39, 51]. The free energy density of the pasta phase is written as

$$f = uf^L(n_p^L, n_n^L, n_e^L) + (1-u)f^G(n_p^G, n_n^G, n_\alpha^G, n_e^G) + f_{\text{surf}}(u, r_D, \tau) + f_{\text{Coul}}(u, r_D, \delta n_c), \quad (8)$$

where u denotes the volume fraction of the liquid phase, L and G represent the liquid and gas phases, respectively. The free energy densities of homogeneous matter in the liquid and gas phases, f^L and f^G , account for the bulk contributions, which can be calculated using Eq. (5). It is noteworthy that α particles may exist as a representative light nucleus in the dilute gas phase, whereas they are absent in the dense liquid phase. Therefore, we include the contributions of α particles in the gas phase, which are treated as non-interacting Boltzmann particles in the present calculation. The last two terms of Eq. (8), f_{surf} and f_{Coul} , represent the surface energy and Coulomb energy, respectively, which arise from the finite-size effects. Here, r_D denotes the size of inner part inside the Wigner-Seitz cell with a geometric dimension D , while τ represents the surface tension. The quantity $\delta n_c = n_c^L - n_c^G$ denotes the charge density difference between the liquid and gas phases.

The finite-size effect plays a crucial role in the studies of pasta phases [41, 48]. We include the surface and Coulomb terms in determining the equilibrium conditions for two-phase coexistence. The surface and Coulomb energy densities are calculated from

$$f_{\text{surf}} = \frac{D\tau u_{\text{in}}}{r_D}, \quad (9)$$

$$f_{\text{Coul}} = \frac{e^2}{2}(\delta n_c)^2 r_D^2 u_{\text{in}} \Phi(u_{\text{in}}), \quad (10)$$

with

$$\Phi(u_{\text{in}}) = \begin{cases} \frac{1}{D+2} \left(\frac{2 - Du_{\text{in}}^{1-2/D}}{D-2} + u_{\text{in}} \right), & D = 1, 3, \\ \frac{u_{\text{in}} - 1 - \ln u_{\text{in}}}{D+2}, & D = 2, \end{cases} \quad (11)$$

where $D = 1, 2, 3$ is the geometric dimension of the cell. u_{in} represents the volume fraction of the inner part, i.e., $u_{\text{in}} = u$ for droplet, rod, and slab configurations, and $u_{\text{in}} = 1 - u$ for tube and bubble configurations. $e = \sqrt{4\pi/137}$ is the electromagnetic coupling constant.

The surface tension τ is an essential quantity that can significantly affect the structure of pasta phases [41, 43]. Generally, τ is achieved by using the Thomas-Fermi approximation for a one-dimensional nuclear system [43, 49]. At finite temperature, both the surface energy and surface entropy are included in the surface tension τ . In the present work, we employ a parameterized surface tension τ , which is a function of the temperature T and the proton fraction in dense phase Y_p^L [47],

$$\tau(Y_p^L, T) = \tau_s h(Y_p^L, T) \frac{2 \cdot 2^\lambda + q}{(Y_p^L)^{-\lambda} + q + (1 - Y_p^L)^{-\lambda}}, \quad (12)$$

with $\tau_s \equiv \tau(0.5, 0)$. The function $h(Y_p^L, T)$ is defined as

$$h(Y_p^L, T) = \begin{cases} \left\{ 1 - [T/T_c(Y_p^L)]^2 \right\}^p, & T \leq T_c(Y_p^L); \\ 0, & T > T_c(Y_p^L). \end{cases} \quad (13)$$

The critical temperature T_c depends on the proton fraction Y_p^L , which is fitted using the function

$$T_c(Y_p^L) = T_{c0} [a_c + b_c \delta^2(Y_p^L) + c_c \delta^4(Y_p^L) + d_c \delta^6(Y_p^L)], \quad (14)$$

where $T_{c0} \equiv T_c(Y_p^L = 0.5)$ is the critical temperature for symmetric nuclear matter and $\delta(Y_p^L) = 1 - 2Y_p^L$ is the neutron excess. The parameterized surface tension τ is determined by fitting numerical results of the Thomas-Fermi approximation for a one-dimensional nuclear system. In Table II, we list the fitted parameters in the surface tension τ for the TM1e and TM1 models.

For a given pasta shape at temperature T and average baryon density n_b , the equilibrium state can be determined by minimizing the total free energy density f described in Eq. (8), which is a function of the following variables: n_p^L , n_n^L , n_e^L , n_p^G , n_n^G , n_e^G , n_α^G , u , and r_D . These variables satisfy the constraints of baryon number conservation and global

TABLE II. Parameters in the surface tension τ for the TM1e and TM1 models.

Model	τ_s (MeV/fm ²)	T_{c0} (MeV)	a_c	b_c	c_c	d_c	q	λ	p
TM1e	1.071	15.6	1.004	-0.273	1.407	-1.421	1.2546	1.8844	1.616
TM1	1.071	15.6	1.076	-1.119	2.985	-2.013	341.5	5.932	1.929

charge neutrality:

$$u(n_p^L + n_n^L) + (1-u)(n_p^G + n_n^G + 4n_\alpha^G) = n_b, \quad (15)$$

$$u(n_p^L - n_e^L) + (1-u)(n_p^G + 2n_\alpha^G - n_e^G) = 0. \quad (16)$$

We introduce the Lagrange multipliers μ_n and μ_e to enforce the constraints and minimize the function,

$$w = f - \mu_n [u(n_p^L + n_n^L) + (1-u)(n_p^G + n_n^G + 4n_\alpha^G)] \\ + \mu_e [u(n_p^L - n_e^L) + (1-u)(n_p^G + 2n_\alpha^G - n_e^G)], \quad (17)$$

which lead to the following equilibrium conditions:

$$\mu_n^G = \mu_n^L, \quad (18)$$

$$\mu_p^G = \mu_p^L + \frac{2f_{\text{Coul}}}{u(1-u)\delta n_c}, \quad (19)$$

$$\mu_e^G = \mu_e^L - \frac{2f_{\text{Coul}}}{u(1-u)\delta n_c}, \quad (20)$$

$$\mu_n^L = \mu_p^L + \mu_e^L, \quad (21)$$

$$\mu_n^G = \mu_p^G + \mu_e^G, \quad (22)$$

$$\mu_\alpha^G = 2\mu_p^G + 2\mu_n^G, \quad (23)$$

$$P^G = P^L + \frac{2f_{\text{Coul}}}{\delta n_c} \left(\frac{n_c^L}{u} + \frac{n_c^G}{1-u} \right) \\ \mp \left[\frac{f_{\text{surf}}}{u_{\text{in}}} + \frac{f_{\text{Coul}}}{u_{\text{in}}} \left(1 + u_{\text{in}} \frac{\Phi'}{\Phi} \right) \right]. \quad (24)$$

The sign in the last equation is “−” for droplet, rod, and slab configurations, while it is “+” for tube and bubble configurations. It is shown in Eqs. (21) and (22) that local β -equilibrium can be reached in both liquid and gas phases. The terms involving f_{Coul} and f_{surf} arise from finite-size effects and reflect the differences between the CLD model and the Gibbs phase equilibrium conditions.

We can obtain the equilibrium condition $f_{\text{surf}} = 2f_{\text{Coul}}$ by minimizing w with respect to r_D . Consequently, the size of the inner part is given by

$$r_D = \left[\frac{D\tau}{e^2(\delta n_c)^2\Phi} \right]^{1/3}, \quad (25)$$

whereas the size of the Wigner-Seitz cell is obtained from

$$r_C = u_{\text{in}}^{-1/D} r_D. \quad (26)$$

In practice, we solve the equilibrium equations at a given temperature T and average baryon density n_b for all pasta

configurations, and then identify the state with the lowest free energy density as the thermodynamically stable phase. When the free energy density of pasta phases is higher than that of uniform matter, the system prefers to have a homogeneous distribution. In the pasta phases, the pressure and chemical potentials of the system may be different from those in the liquid and gas phases due to finite-size effects. Therefore, we compute these quantities by the thermodynamic relations.

III. RESULTS AND DISCUSSION

A. Nuclear pasta in hot neutron-star matter

We first investigate the pasta phases appearing in nuclear matter under β -equilibrium at finite temperature, which is considered to occur in the crust of a PNS. To describe these pasta phases, we employ the CLD model, in which a dense nuclear liquid coexists with a dilute gas across a sharp interface. For the nuclear interaction, we adopt the TM1e model with a small symmetry energy slope $L = 40$ MeV, which is compatible with both nuclear experimental data and recent astrophysical observations of neutron stars. To examine the impact of nuclear symmetry energy, we compare the results of TM1e to those of the original TM1 model, which has a larger slope $L = 110.8$ MeV. It is noteworthy that the two models differ only in their isovector parts, while their isoscalar properties are identical.

At a given temperature T and average baryon density n_b , we perform calculations for all configurations including both uniform matter and nonuniform pasta phases, and then identify the one with the lowest free energy density as the thermodynamically stable phase. In Fig. 3, we show the phase diagrams in the n_b - T plane obtained with the TM1e model (left panel) and compare them with those of the TM1 model (right panel). The blue solid lines correspond to isentropic trajectories with entropy per baryon $S = 0.5, 1, 2$. Inside the nonuniform matter region, the values of S are taken to be the cell-averaged entropy per baryon. One can see that the TM1e model predicts various pasta shapes at low temperatures (left panel), while the TM1 model yields only droplet configurations (right panel). This difference arises because the symmetry energy slope L can significantly influence the emergence of pasta phases. A similar correlation between L and pasta phases has also been observed in the studies of the neutron-star inner crust [35]. In the left panel of Fig. 3, we observe that various pasta configurations emerge sequentially with increasing density, while the transitions between different shapes are

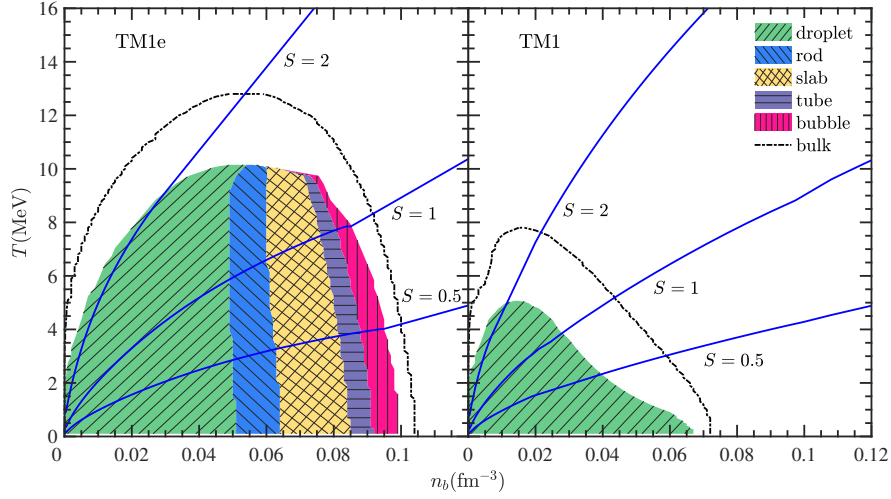


FIG. 3. Phase diagrams in the n_b - T plane obtained in the CLD method using the TM1e and TM1 models. Different colors indicate the regions for different pasta shapes. The black dot-dashed lines indicate the boundary of nonuniform matter obtained from a bulk calculation without finite-size effects. The blue solid lines correspond to isentropic trajectories with entropy per baryon $S = 0.5, 1, 2$.

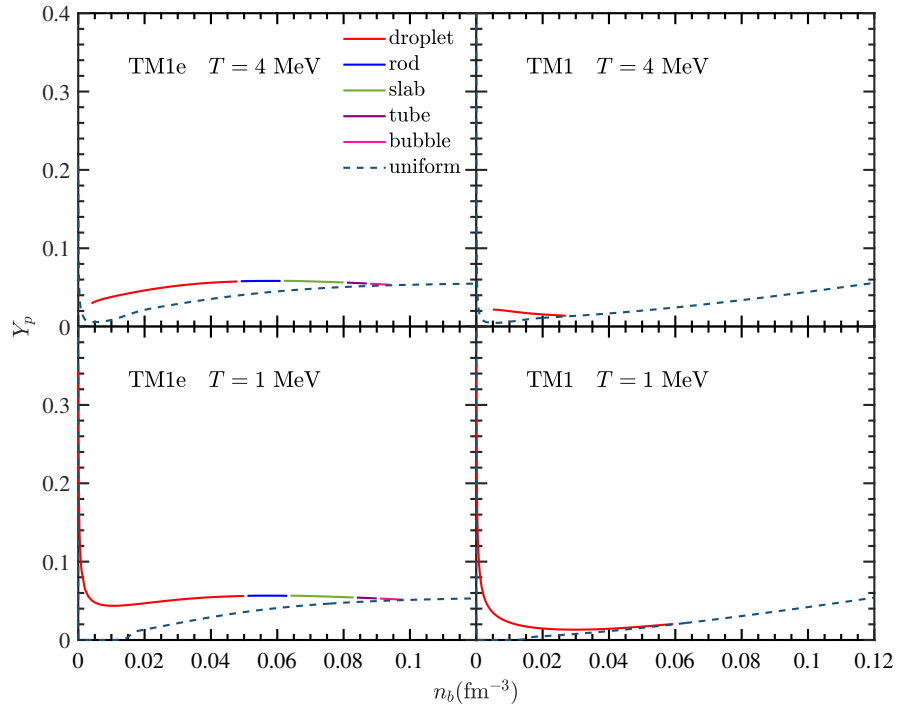


FIG. 4. Average proton fraction Y_p as a function of the baryon density n_b in the matter under the conditions of charge neutrality and β -equilibrium. The results for the TM1e and TM1 models are shown in the left and right panels, respectively. The dashed lines indicate the proton fraction of uniform matter.

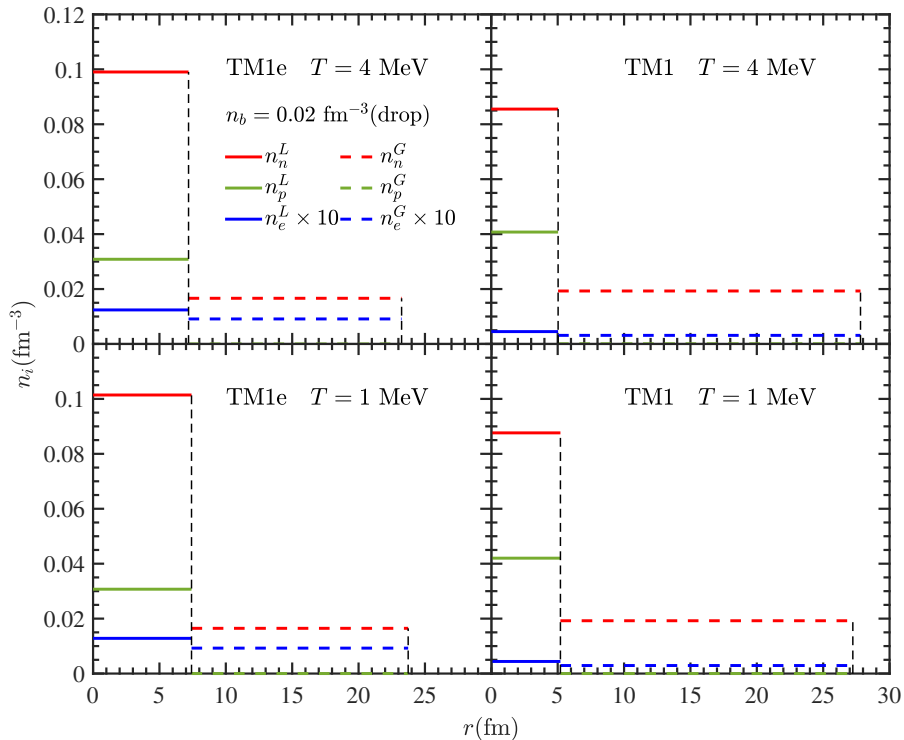


FIG. 5. Density profiles of nucleons and electrons within the Wigner-Seitz cell for a droplet configuration at $n_b = 0.02 \text{ fm}^{-3}$. The results obtained with the TM1e and TM1 models are shown in the left and right panels, respectively. The cell boundary and the sharp interface between the liquid and gas phases are indicated by the vertical dashed lines.

only weakly dependent on temperature T . As the temperature increases, the density range of nonuniform matter shrinks. Eventually, when the temperature reaches the critical value T_c , the nonuniform matter phase disappears completely. In contrast, in the right panel, the critical value T_c and nonuniform matter region for the TM1 model are obviously smaller than those for the TM1e model. This difference can be attributed to the different symmetry energy slopes in these two models, which significantly influence the properties of β -equilibrium matter. The black dot-dashed lines indicate the boundary of bulk calculations, where the finite-size effects, such as surface and Coulomb contributions, are neglected. Notably, the finite-size effects can significantly reduce the nonuniform matter region.

In Fig. 4, we show the average proton fraction Y_p as a function of the baryon density n_b in the matter under the conditions of charge neutrality and β -equilibrium. The results of the TM1e model (left panels) at $T = 1$ and 4 MeV are compared with those in the TM1 model (right panels). Because of different symmetry energy behaviors shown in Fig. 2, Y_p in the TM1e model is significantly larger than that in the TM1 model. Generally, a larger symmetry energy E_{sym} favors more symmetric nuclear matter, yielding larger proton fraction Y_p at corresponding densities. In nonuniform matter, the proton fraction in the dense liquid phase (Y_p^L) is much

larger than that in the gas phase (Y_p^G). Consequently, the average proton fraction Y_p of the pasta phases (colored solid lines) is higher than that of uniform matter (dashed lines). Furthermore, the results exhibit only a weak dependence on the temperature T . At $T = 1$ MeV, Y_p of nonuniform matter rises rapidly with decreasing density for $n_b < 0.05 \text{ fm}^{-3}$. This trend is not observed at $T = 4$ MeV, since the onset of nonuniform matter occurs at a density of about 0.05 fm^{-3} in this case.

To analyze the equilibrium between the liquid and gas phases, we plot in Fig. 5 the particle density profiles within the Wigner-Seitz cell for a droplet configuration at $n_b = 0.02 \text{ fm}^{-3}$. Particle densities in the dense liquid phase are shown by colored solid lines, while those in the dilute gas phase are represented by colored dashed lines. The cell boundary and the sharp interface between the liquid and gas phases are indicated by the vertical dashed lines. The dense liquid phase has a higher proton density (n_p^L) than the electron density (n_e^L), so it is positively charged. In contrast, the dilute gas phase is negatively charged. Furthermore, the electron density in the liquid phase (n_e^L) slightly exceeds that in the gas phase (n_e^G). This arises from the charge screening effect, which tends to reduce the net charge density in each phase to minimize the Coulomb energy. The proton density in the gas phase (n_p^G) is significantly lower, which implies its

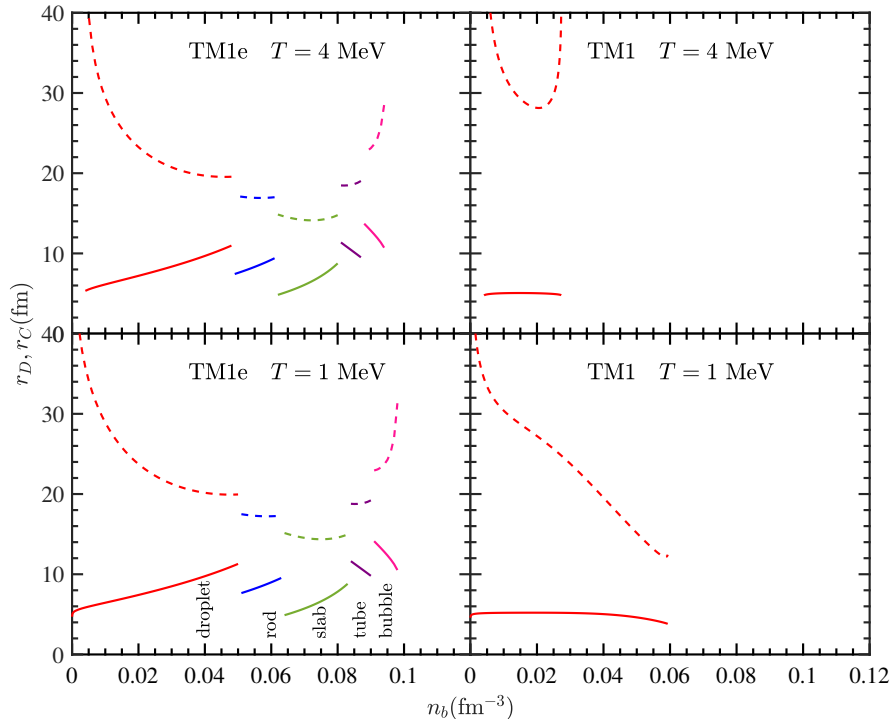


FIG. 6. Size of the Wigner-Seitz cell r_C (dashed lines) and that of the inner phase r_D (solid lines) as a function of the baryon density n_b . The results obtained with the TM1e and TM1 models are shown in the left and right panels, respectively.

proton fraction (Y_p^G) is much smaller than that in the liquid phase (Y_p^L). Comparing with the results in the TM1 model (right panels), the TM1e model yields larger nuclear radius (r_D), higher neutron density (n_n^L), and lower proton density (n_p^L). These trends are attributed to the different symmetry-energy behaviors shown in Fig. 2. A comparison of the upper and lower panels shows that the dependence on temperature T is weak.

In Fig. 6 we show the size of the Wigner-Seitz cell r_C (dashed lines) and that of the inner phase r_D (solid lines) as a function of the baryon density n_b . Compared with various pasta phases obtained in the TM1e model (left panels), the TM1 model predicts only droplet configurations (right panels). In the left panels, we see that r_D in the droplet, rod and slab phases increases with increasing n_b , whereas it decreases in the tube and bubble phases. The cell size r_C exhibits the opposite trend. This behavior is consistent with an increasing volume fraction of the liquid phase obtained in the TM1e model (see the left panels of Fig. 7). In the right panels, the results for $T = 4$ MeV are significantly different from those for $T = 1$ MeV. The density range of the droplet configuration for $T = 4$ MeV is appreciably smaller than that for $T = 1$ MeV. This is consistent with the phase diagrams shown in Fig. 3. We display in Fig. 7 the volume fraction of the liquid phase u as a function of the baryon density n_b . The black dot-dashed lines correspond to the bulk equilibrium results, where finite-size effects are neglected. These effects are more pronounced

in the TM1 model (right panels) than in the TM1e model (left panels). It is shown that in the TM1e model, u monotonically increases with increasing n_b . In contrast, u in the TM1 model exhibits a non-monotonic feature, where u reaches a maximum and then declines, implying that the nonuniform matter leaves the coexistence region in the dilute gas phase. This feature, called retrograde condensation [52, 53], becomes more pronounced at higher temperatures.

In Fig. 8, we display the free energy per baryon, F , as a function of the baryon density n_b . The results shown by dashed lines for uniform matter are significantly higher than those represented by solid lines for nonuniform pasta phases, implying that the formation of pasta structures lowers the free energy at subsaturation densities. On the other hand, the results of bulk equilibrium calculations shown by dot-dashed lines are lower than those of pasta phases, because the positive contributions from the surface and Coulomb terms are neglected in the bulk equilibrium approach. The differences among these results are more pronounced at $T = 1$ MeV (lower panels) than at $T = 4$ MeV (upper panels), since the finite-size effects play a more important role at lower temperatures. A comparison of the results in the TM1e model (left panels) with those in the TM1 model (right panels) shows that their trends are very similar, although quantitative differences remain. In Fig. 9, we present the pressure P as a function of the baryon density n_b . Compared to the TM1 model (right panels), the TM1e model (left panels) shows larger differences

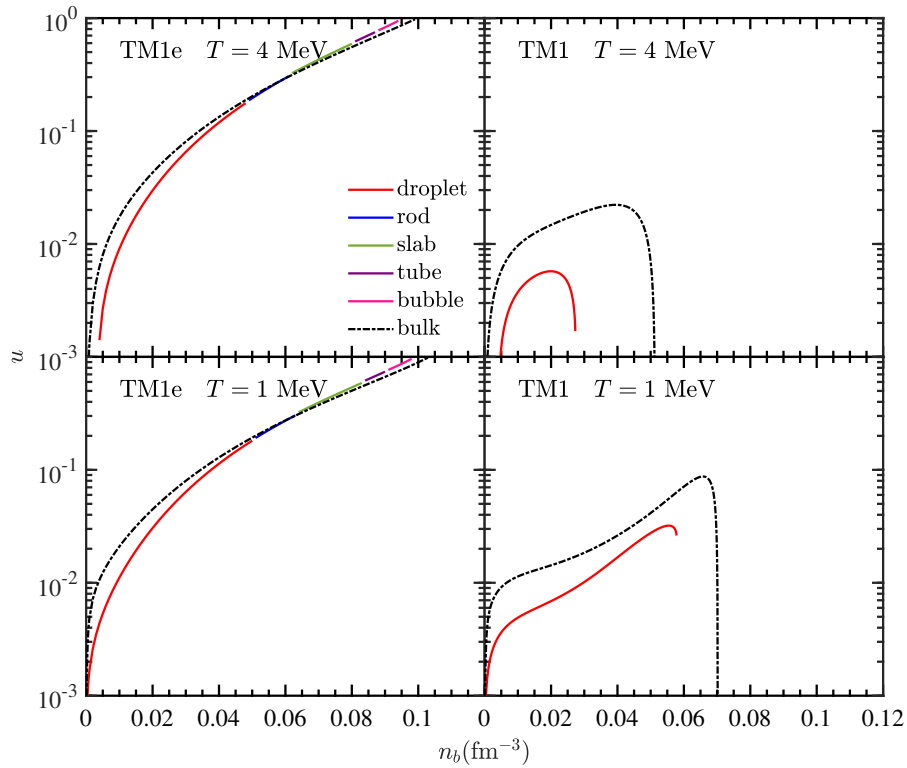


FIG. 7. Volume fraction u as a function of the baryon density n_b . The black dot-dashed lines correspond to the bulk equilibrium results.

between uniform matter and nonuniform pasta phases. This is because the TM1e model predicts a larger pasta region (see Fig. 3) and a larger volume fraction u (see Fig. 7), implying that pasta structures play a more important role in the TM1e case.

B. Existence of nuclear pasta in a PNS

We investigate the influence of pasta phases on the macroscopic properties of PNSs, where a constant entropy approach is adopted. We consider the neutrino-free stage of PNSs with fixed entropy per baryon S . In Fig. 10, we show the isentropic EOS for $S = 0.5, 1, 2$, along with the $S = 0$ curve corresponding to the zero temperature case for comparison. As indicated in the phase diagram (Fig. 3), the temperature T along the isentropic trajectories (blue solid lines) decreases with decreasing baryon density n_b . The system enters the nonuniform matter region at lower densities, corresponding to the inner crust of the star. For the outer crust, we adopt the zero-temperature BPS EOS, as the temperature in this regime is negligible. In Fig. 10, the black square indicates the junction between the BPS EOS and the inner crust segments, while the colored circle marks the crust-core transition. It is observed that for a given energy density, the pressure P decreases monotonically with decreasing entropy S .

Using the isentropic EOS shown in Fig. 10, we solve the well-known Tolman–Oppenheimer–Volkoff (TOV) equation to obtain the properties of PNSs. In Fig. 11, the mass-radius relations of PNSs are shown for entropy per baryon $S = 0, 0.5, 1, 2$. It is found that as S increases, both the maximum mass and the corresponding radius increase, and the mass-radius curve becomes flatter. This implies that PNSs contract with the decrease of S during the cooling process. In particular, the radii of lower-mass stars exhibit stronger sensitivity to S . In Fig. 12, we show the temperature profiles of a canonical $1.4 M_\odot$ PNS, calculated using the constant entropy approach with $S = 0.5, 1, 2$. It is found that the central density n_c increases as S decreases. For a fixed value of S , the temperature decreases with increasing radial coordinate r . Overall, a higher S corresponds to higher temperatures in the stellar interior.

To investigate the influence of pasta phases on the macroscopic properties of PNSs, we plot in Fig. 13 the mass-radius relation obtained using the isentropic EOS for $S = 1$ with pasta phases appearing in the inner crust, and compare it with that obtained using the EOS of uniform matter without pasta phases. It is observed that the radii with pasta phases are larger than those without pasta phases, and this difference is more pronounced for lower-mass stars. This can be attributed to higher pressures in the presence of nonuniform pasta phases, compared to the uniform matter case (see the left panels of

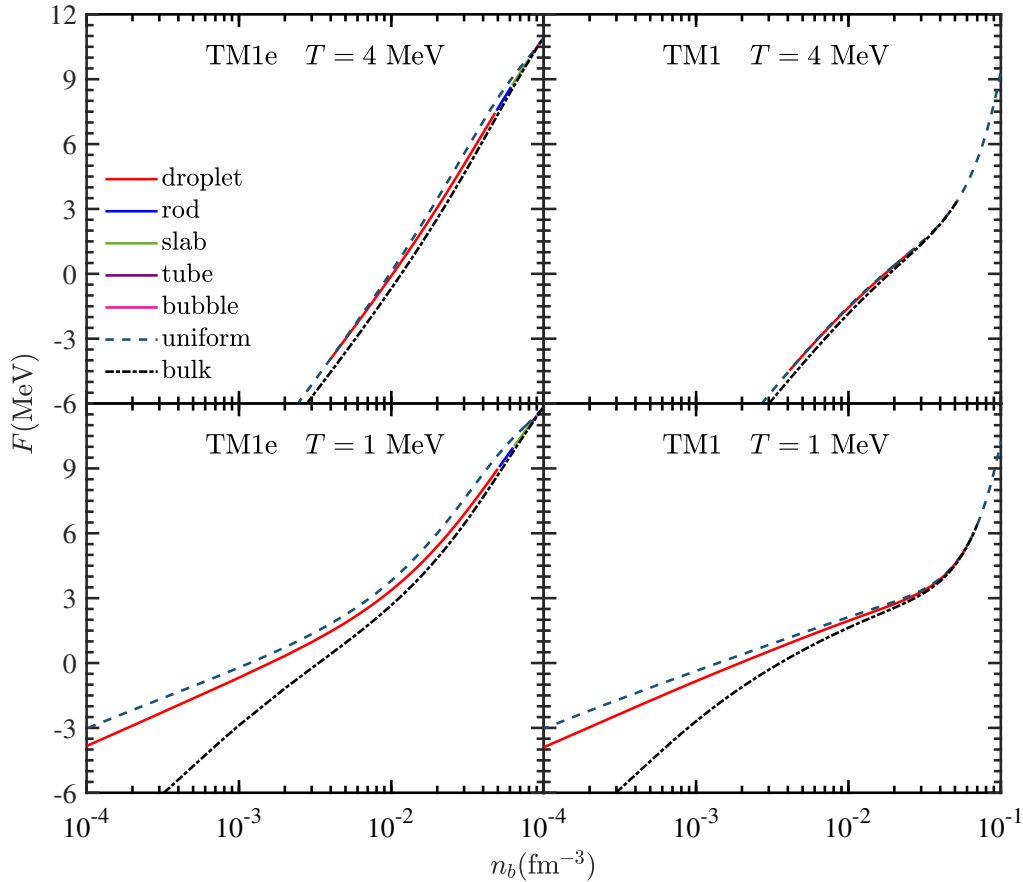


FIG. 8. Free energy per baryon F as a function of the baryon density n_b . The dashed lines correspond to the results for uniform matter, while the dot-dashed lines indicate those from bulk equilibrium calculations.

Fig. 9). In Fig. 14, we show the density profiles in the surface region of a canonical $1.4 M_\odot$ PNS. In the case with pasta phases, the red vertical dot-dashed line at $r \simeq 12.1$ km indicates the boundary between the uniform core and the inner crust, whereas the boundary between the inner crust and the outer crust is indicated by the red dotted line at $r \simeq 13.3$ km. Therefore, pasta phases exist in the inner crust, which has a thickness of about 1.2 km. In the case without pasta phases, we use the uniform EOS until $r \simeq 13.2$ km, where the core connects directly to the outer crust marked by the blue vertical dotted line. In both cases, the outer crust exhibits similar behavior, but the presence of pasta phases in the inner crust pushes the outer crust to larger radii. Furthermore, the pasta phases may change the thermal conductivity and influence the thermal evolution of the star [54].

IV. CONCLUSIONS

In this work, we have investigated the properties of nuclear pasta appearing in hot neutron-star matter. We employed the

CLD method to describe the pasta phases with various geometric shapes. In the CLD method, the Wigner-Seitz approximation was employed to simplify the calculations, where the whole space was divided into equivalent cells of specific geometric symmetry. The matter in each cell consists of a dense liquid phase and a dilute gas phase separated by a sharp interface. We employed a parametrized surface tension τ dependent on temperature and isospin asymmetry, with the parameters adjusted to match the results from the Thomas-Fermi approximation for a one-dimensional nuclear system. We have derived the equilibrium conditions for two coexisting phases by minimizing the total free energy, which includes surface and Coulomb contributions. These conditions, incorporating finite-size effects, differ from the Gibbs conditions for phase equilibrium. When finite-size effects are neglected, the CLD method reduces to a bulk matter calculation that satisfies the Gibbs equilibrium conditions.

For the nuclear interaction, we have employed RMF models with different symmetry energy slopes. We found that the TM1e model with a small symmetry energy slope $L = 40$ MeV predicted various pasta shapes at low temperatures,

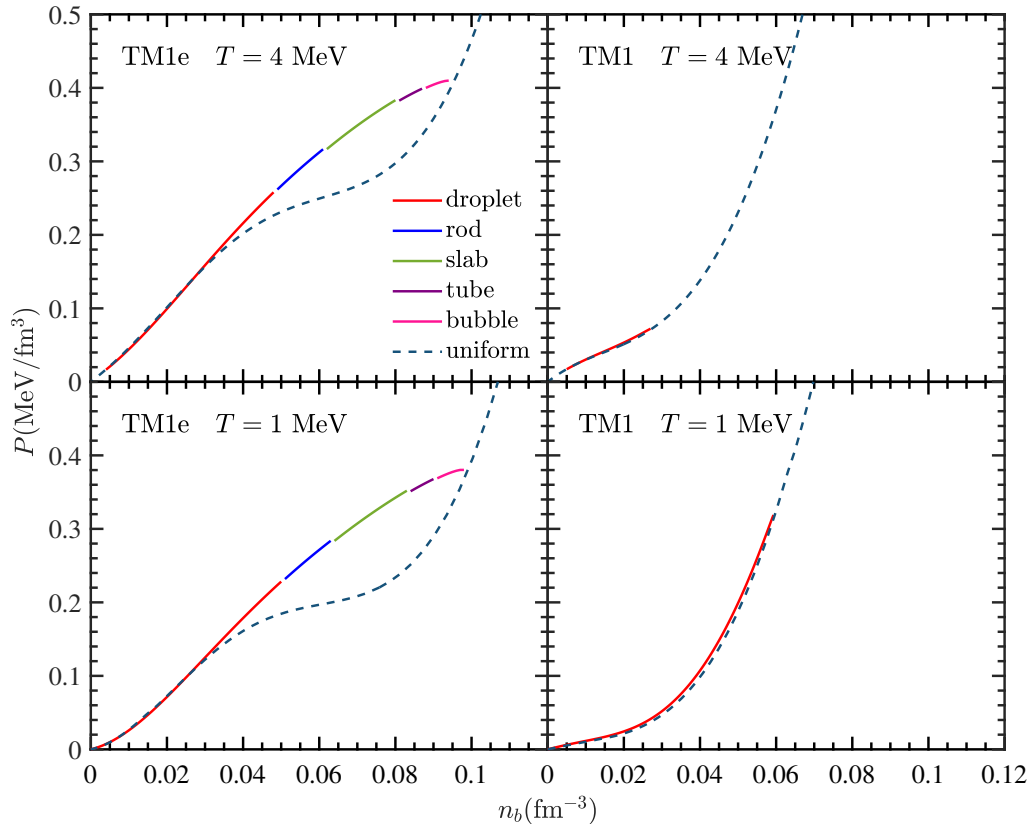


FIG. 9. Pressure P as a function of the baryon density n_b . The results of pasta phases (colored solid lines) are compared with those of uniform matter (dashed lines).

while the TM1 model with $L = 110.8$ MeV yielded only the droplet configuration up to the crust-core transition density. In addition, the properties of nonuniform neutron-star matter exhibit significant differences between the TM1e and TM1 models. It is noteworthy that the TM1e and TM1 models have the same isoscalar properties but exhibit different behaviors regarding nuclear symmetry energy. Therefore, the comparison between these two models reflects the influence solely from the symmetry energy without interference of the isoscalar part.

We have explored the occurrence and influence of nuclear pasta in a PNS, employing a constant entropy approach. Using the isentropic EOS in the TM1e model, we have solved the TOV equation to obtain the properties of the PNS. The nuclear pasta phases appeared in the inner crust with a thick-

ness of about 1.2 km. Compared to results without pasta phases, PNS radii with pasta phases are slightly larger, and this difference is more pronounced for lower-mass stars. In the present calculations, we considered only neutrino-free matter in β -equilibrium, corresponding to the later stages of the PNS cooling process. Pasta phases in hot neutron-star matter with trapped neutrinos will be investigated in future work.

V. ACKNOWLEDGMENTS

This work was supported by the National Natural Science Foundation of China under Grants Nos. 12475149 and 12175109, and by Guangdong Basic and Applied Basic Research Foundation (Grant No: 2024A1515010911).

-
- [1] T. Fischer, S. C. Whitehouse, A. Mezzacappa, F. K. Thielemann, and M. Liebendorfer, *Astronomy & Astrophysics* **517**, A80 (2010).
 [2] A. Burrows, *Reviews of Modern Physics* **85**, 245 (2013).

- [3] S. Yamada, H. Nagakura, R. Akaho, A. Harada, S. Furusawa, W. Iwakami, H. Okawa, H. Matsufuru, and K. Sumiyoshi, *Proceedings of the Japan Academy, Series B* **100**, 190 (2024).
 [4] K. Sumiyoshi, K. ichiro Nakazato, H. Suzuki, J. Hu, and H. Shen, *The Astrophysical Journal* **887**, 110 (2019).

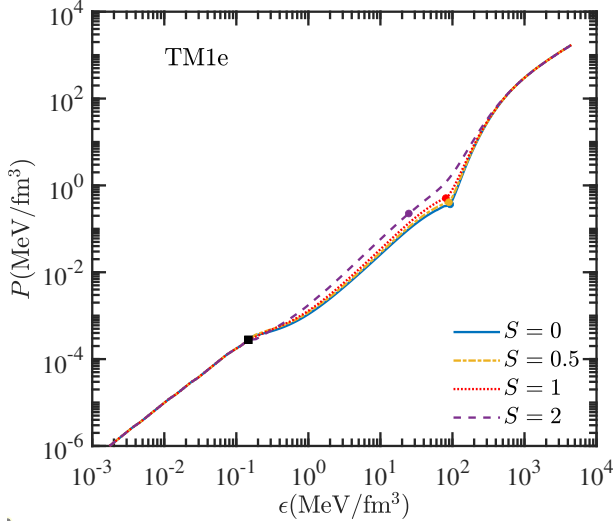


FIG. 10. Pressure P as a function of the energy density ϵ for several values of entropy per baryon S obtained in the TM1e model. The cold BPS EOS is adopted for the outer crust, and the matching point to the inner crust is marked by the black square. The crust-core transition is indicated by the colored circles.

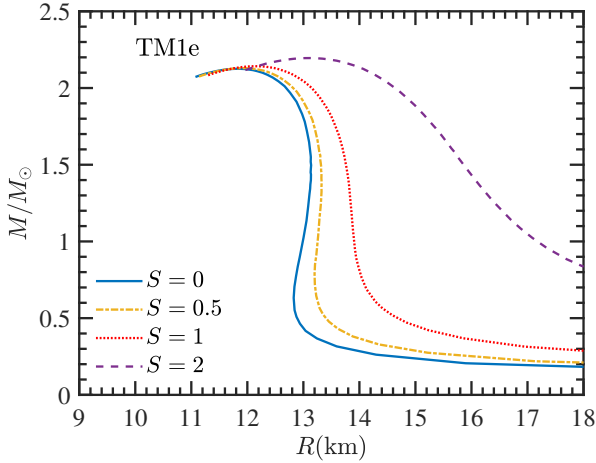


FIG. 11. Mass-radius relations of PNSs obtained using the isentropic EOS shown in Fig. 10.

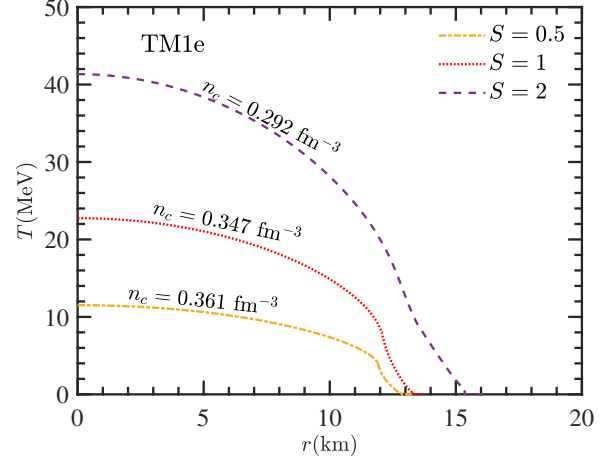


FIG. 12. Temperature profiles of a canonical $1.4 M_{\odot}$ PNS obtained with the constant entropy approach for $S = 0.5, 1, 2$. The corresponding central density n_c increases as S decreases.

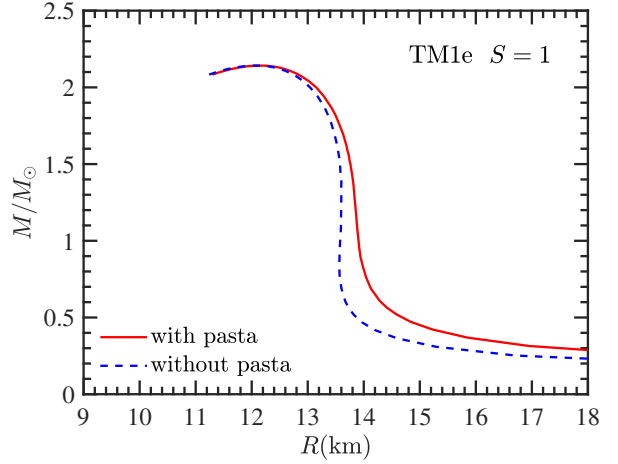


FIG. 13. Mass-radius relations obtained using the isentropic EOS for $S = 1$, including pasta phases in the inner crust (red solid line). The results without pasta phases (blue dashed line) are shown for comparison.

[5] K. Nakazato and H. Suzuki, *The Astrophysical Journal* **878**, 25 (2019).
 [6] K. Nakazato, H. Suzuki, and H. Togashi, *Physical Review C* **97**, 035804 (2018).
 [7] A. Y. Potekhin and G. Chabrier, *Astronomy & Astrophysics* **645**, A102 (2021).
 [8] N. Chamel and P. Haensel, *Living Reviews in Relativity* **11**, 10 (2008).
 [9] J. M. Lattimer and M. Prakash, *Physics Reports* **621**, 127 (2016), memorial Volume in Honor of Gerald E. Brown.
 [10] M. Oertel, M. Hempel, T. Klähn, and S. Typel, *Reviews of Modern Physics* **89**, 015007 (2017).
 [11] H. Koehn, H. Rose, P. T. H. Pang, R. Somasundaram, B. T. Reed, I. Tews, A. Abac, O. Komoltsev, N. Kunert, A. Kurkela,

M. W. Coughlin, B. F. Healy, and T. Dietrich, *Physical Review X* **15**, 021014 (2025).
 [12] K. Chatziioannou, H. T. Cromartie, S. Gandolfi, I. Tews, D. Radice, A. W. Steiner, and A. L. Watts, *Reviews of Modern Physics* **97**, 045007 (2025).
 [13] S. Ascenzi, V. Graber, and N. Rea, *Astroparticle Physics* **158**, 102935 (2024).
 [14] B. P. Abbott, R. Abbott, T. D. Abbott, M. R. Abernathy, F. Acernese, K. Ackley, C. Adams, T. Adams, P. Addesso, *et al.* (LIGO Scientific Collaboration and Virgo Collaboration), *Physical Review Letters* **116**, 061102 (2016).
 [15] B. P. Abbott, R. Abbott, T. Abbott, F. Acernese, K. Ackley, C. Adams, T. Adams, P. Addesso, R. Adhikari, V. B. Adya, *et al.*, *Physical Review Letters* **119**, 161101 (2017).
 [16] B. P. Abbott, R. Abbott, T. Abbott, F. Acernese, K. Ackley, C. Adams, T. Adams, P. Addesso, R. X. Adhikari, V. B. Adya,

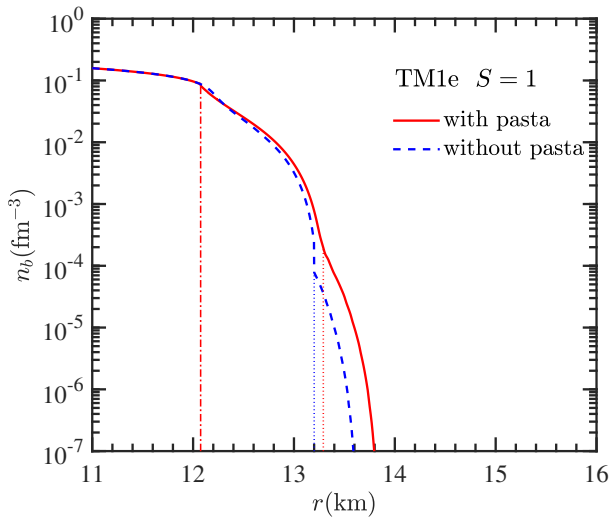


FIG. 14. Density profiles in the surface region of a canonical $1.4 M_{\odot}$ PNS for $S = 1$. The red vertical dot-dashed line indicates the boundary between the uniform core and the inner crust, whereas the red dotted line marks the boundary between the inner crust and the outer crust. In the case without pasta phases, the uniform EOS is employed until $r \simeq 13.2$ km, where the core connects directly to the outer crust indicated by the blue vertical dotted line.

- et al.*, *Physical Review Letters* **121**, 161101 (2018).
- [17] F. J. Fattoyev, J. Piekarewicz, and C. J. Horowitz, *Physical Review Letters* **120**, 172702 (2018).
- [18] E. R. Most, L. R. Weih, L. Rezzolla, and J. Schaffner-Bielich, *Physical Review Letters* **120**, 261103 (2018).
- [19] P. Landry, R. Essick, and K. Chatziioannou, *Physical Review D* **101**, 123007 (2020).
- [20] K. Chatziioannou, *General Relativity and Gravitation* **52**, 109 (2020).
- [21] P. B. Demorest, T. Pennucci, S. Ransom, M. Roberts, and J. Hessels, *Nature* **467**, 1081 (2010).
- [22] Z. Arzoumanian, A. Brazier, S. Burke-Spolaor, S. Chamberlin, S. Chatterjee, B. Christy, J. M. Cordes, N. J. Cornish, F. Crawford, H. T. Cromartie, K. Crowter, M. E. DeCesar, P. B. Demorest, T. Dolch, J. A. Ellis, R. D. Ferdman, E. C. Ferrara, E. Fonseca, N. Garver-Daniels, P. A. Gentile, D. Halmrast, E. A. Huerta, F. A. Jenet, C. Jessup, G. Jones, M. L. Jones, D. L. Kaplan, M. T. Lam, T. J. W. Lazio, L. Levin, A. Lommen, D. R. Lorimer, J. Luo, R. S. Lynch, D. Madison, A. M. Matthews, M. A. McLaughlin, S. T. McWilliams, C. Mingarelli, C. Ng, D. J. Nice, T. T. Pennucci, S. M. Ransom, P. S. Ray, X. Siemens, J. Simon, R. Spiewak, I. H. Stairs, D. R. Stinebring, K. Stovall, J. K. Swiggum, S. R. Taylor, M. Vallisneri, R. van Haasteren, S. J. Vigeland, W. Zhu, and T. N. Collaboration, *The Astrophysical Journal Supplement Series* **235**, 37 (2018).
- [23] J. Antoniadis, P. C. C. Freire, N. Wex, T. M. Tauris, R. S. Lynch, M. H. van Kerkwijk, M. Kramer, C. Bassa, V. S. Dhillon, T. Driebe, J. W. T. Hessels, V. M. Kaspi, V. I. Kondratiev, N. Langer, T. R. Marsh, M. A. McLaughlin, T. T. Pennucci, S. M. Ransom, I. H. Stairs, J. van Leeuwen, J. P. W. Verbiest, and D. G. Whelan, *Science* **340**, 1233232 (2013).
- [24] E. Fonseca, H. T. Cromartie, T. T. Pennucci, P. S. Ray, A. Y. Kirichenko, S. M. Ransom, P. B. Demorest, I. H. Stairs, Z. Arzoumanian, L. Guillemot, A. Parthasarathy, M. Kerr, I. Cognard, P. T. Baker, H. Blumer, P. R. Brook, M. DeCesar, T. Dolch, F. A. Dong, E. C. Ferrara, W. Fiore, N. Garver-Daniels, D. C. Good, R. Jennings, M. L. Jones, V. M. Kaspi, M. T. Lam, D. R. Lorimer, J. Luo, A. McEwen, J. W. McKee, M. A. McLaughlin, N. McMann, B. W. Meyers, A. Naidu, C. Ng, D. J. Nice, N. Pol, H. A. Radovan, B. Shapiro-Albert, C. M. Tan, S. P. Tendulkar, J. K. Swiggum, H. M. Wahl, and W. W. Zhu, *The Astrophysical Journal Letters* **915**, L12 (2021).
- [25] M. C. Miller, F. K. Lamb, A. J. Dittmann, S. Bogdanov, Z. Arzoumanian, K. C. Gendreau, S. Guillot, A. Harding, W. Ho, J. M. Lattimer, *et al.*, *The Astrophysical Journal Letters* **887**, L24 (2019).
- [26] T. E. Riley, A. L. Watts, S. Bogdanov, P. S. Ray, R. M. Ludlam, S. Guillot, Z. Arzoumanian, C. L. Baker, A. V. Bilous, D. Chakrabarty, *et al.*, *The Astrophysical Journal Letters* **887**, L21 (2019).
- [27] M. C. Miller, F. K. Lamb, A. J. Dittmann, S. Bogdanov, Z. Arzoumanian, K. C. Gendreau, S. Guillot, W. C. G. Ho, J. M. Lattimer, M. Loewenstein, *et al.*, *The Astrophysical Journal Letters* **918**, L28 (2021).
- [28] T. E. Riley, A. L. Watts, P. S. Ray, S. Bogdanov, S. Guillot, S. M. Morsink, A. V. Bilous, Z. Arzoumanian, D. Choudhury, J. S. Deneva, *et al.*, *The Astrophysical Journal Letters* **918**, L27 (2021).
- [29] M. Dutra, O. Lourenço, S. Avancini, B. V. Carlson, A. Delfino, D. Menezes, C. Providência, S. Typel, and J. Stone, *Physical Review C* **90**, 055203 (2014).
- [30] T. Miyatsu, M.-K. Cheoun, K. Kim, and K. Saito, *Frontiers in Physics* **12**, 1531475 (2025).
- [31] Y. Sugahara and H. Toki, *Nuclear Physics A* **579**, 557 (1994).
- [32] S. Bao, J. Hu, Z. Zhang, and H. Shen, *Physical Review C* **90**, 045802 (2014).
- [33] F. Ji, J. Hu, S. Bao, and H. Shen, *Physical Review C* **100**, 045801 (2019).
- [34] H. Shen, F. Ji, J. Hu, and K. Sumiyoshi, *The Astrophysical Journal* **891**, 148 (2020).
- [35] S. Bao and H. Shen, *Physical Review C* **91**, 015807 (2015).
- [36] S. Li, J. Pang, H. Shen, J. Hu, and K. Sumiyoshi, *The Astrophysical Journal* **980**, 54 (2025).
- [37] D. G. Ravenhall, C. J. Pethick, and J. R. Wilson, *Physical Review Letters* **50**, 2066 (1983).
- [38] M. Okamoto, T. Maruyama, K. Yabana, and T. Tatsumi, *Physical Review C* **88**, 025801 (2013).
- [39] H. Shen, H. Toki, K. Oyamatsu, and K. Sumiyoshi, *The Astrophysical Journal Supplement Series* **197**, 20 (2011).
- [40] G. Watanabe, K. Iida, and K. Sato, *Nuclear Physics A* **676**, 455 (2000).
- [41] F. Ji, J. Hu, S. Bao, and H. Shen, *Physical Review C* **102**, 015806 (2020).
- [42] K. Oyamatsu and K. Iida, *Physical Review C* **75**, 015801 (2007).
- [43] S. S. Avancini, S. Chiacchiera, D. P. Menezes, and C. m. c. Providência, *Physical Review C* **82**, 055807 (2010).
- [44] F. Grill, C. m. c. Providência, and S. S. Avancini, *Physical Review C* **85**, 055808 (2012).
- [45] H. Pais, S. Chiacchiera, and C. m. c. Providência, *Physical Review C* **91**, 055801 (2015).
- [46] C.-J. Xia, T. Maruyama, N. Yasutake, and T. Tatsumi, *Physical Review D* **106**, 063020 (2022).
- [47] A. S. Schneider, L. F. Roberts, and C. D. Ott, *Physical Review C* **96**, 065802 (2017).
- [48] S. Bao and H. Shen, *Physical Review C* **93**, 025807 (2016).
- [49] S. Bao and H. Shen, *Physical Review C* **89**, 045807 (2014).

- [50] H. Shen, H. Toki, K. Oyamatsu, and K. Sumiyoshi, *Progress of Theoretical Physics* **100**, 1013 (1998).
- [51] J. M. Lattimer and F. D. Swesty, *Nuclear Physics A* **535**, 331 (1991).
- [52] H. Müller and B. D. Serot, *Physical Review C* **52**, 2072 (1995).
- [53] A. Roggero, J. Margueron, L. F. Roberts, and S. Reddy, *Physical Review C* **97**, 045804 (2018).
- [54] S. Ghosh, S. Shaikh, P. J. Kalita, P. Routaray, B. Kumar, and B. Agrawal, *Nuclear Physics B* **1008**, 116697 (2024).